

EFFECTS OF THE HORIZONTAL SCALES OF THE CLOUD-RESOLVING MODEL ON TROPICAL CYCLONES IN A MULTISCALE MODELING FRAMEWORK

Kuan-Ting Kuo*, Chien-Ming Wu, Wei-Ting Chen
Department of Atmospheric Sciences, National Taiwan University, Taipei, Taiwan

1. INTRODUCTION

Tropical cyclones (TCs) pose significant threats to low- and mid-latitude coastal areas, making their accurate simulation in general circulation models (GCMs) crucial. However, despite advancements in model resolution, TC simulation remains challenging, with considerable variability in frequency across different GCMs (Roberts et al., 2020). Knutson et al. (2020) reviewed literature on future TC activity projections and found high or medium-to-high confidence in increased TC precipitation rates under 2 °C global warming. Regarding TC frequency, while many GCMs project a decrease with warming (e.g., Held and Zhao, 2011), observational evidence for this trend is inconclusive. Model biases and limitations in capturing interactions between TCs and the large-scale environment may contribute to these discrepancies. Emanuel (2021) utilized downscaling techniques to predict a rising trend in TC frequency with climate warming, raising concerns about GCMs' ability to accurately simulate TC behavior. Therefore, understanding the processes influencing TC frequency in GCMs is critical for improving confidence in future climate projections.

The limitations of horizontal resolution in GCMs contribute to uncertainties in simulating TC frequency. Villafuerte et al. (2021) demonstrated that variations in convective parameterizations can lead to significant differences in TC numbers, ranging from 1.2 to 22.5 TCs per year. Moreover, altering the physics timestep can influence TC frequency by affecting convective available potential energy (CAPE) removal and grid-scale vertical mass flux (Zarzycki, 2022). Zhao et al. (2012) found that TC frequency is sensitive to model parameters like cumulus lateral mixing rate and divergence damping. These studies highlight the substantial impact of conventional parameterizations on TC frequency. However, assessing parameter tuning's correctness poses challenges. Parameter tuning that overlooks sub-grid processes may result in overfitting to present climate conditions and inaccurate future climate projections. To address this issue, we adopt a convective-permitting approach within a GCM in the Multiscale Modeling Framework (MMF).

The MMF or Superparameterization (SP) replaces the conventional cumulus parameterization in each grid column with a nested integration of two-dimensional cloud-resolving models (CRMs) to explicitly simulate convection at the grid scale. The Superparameterized Community Atmosphere Model (SPCAM) is a GCM with SP developed by Khairoutdinov and Randall (2001) based on the Community Atmosphere Model (CAM) from the National Center of Atmospheric Research (NCAR). Previous studies have demonstrated enhancements in simulating various phenomena such as diurnal variation of rainfall (Khairoutdinov et al., 2005; Zhang et al., 2008; Pritchard and Somerville, 2009), the Madden-Julian Oscillation (Benedict and Randall, 2009), low-level moistening before major precipitation events (DeMott et al., 2007), and the mean state of the Asian summer monsoon (DeMott et al., 2011). Additionally, the South China Sea summer monsoon, a sub-system of the Asian summer monsoon, has been investigated using this model (Kuo, Chen, and Wu, 2020). With these advancements, SPCAM is well-suited for studying multiscale weather systems where convection plays a pivotal role. However, it is acknowledged that SPCAM tends to produce precipitation hotspots over the Asian summer monsoon region and the western North Pacific in climate simulations (Khairoutdinov et al., 2005; Randall et al., 2016). This bias may be partially attributed to tropical cyclones. Therefore, in this study, we aim to utilize SPCAM to explore model sensitivities in simulating tropical cyclone activities over the western North Pacific.

GCMs with SP offer the advantage of explicitly calculating cloud-scale statistics from CRMs without relying on physical or empirical assumptions for diagnosing the grid-scale environment. Different CRM configurations may yield specific cloud distributions or convective characteristics. In an early sensitivity test, Khairoutdinov and Randall (2001) examined four configurations with an 18-day simulation in a CRM, integrated into SPCAM. They found that changes in geometry (2D or 3D), domain size, and resolution did not exhibit clear biases, and all experiments performed consistently. However, this study only evaluated CRM performance with prescribed large-scale forcing, omitting interaction between the large-scale and sub-grid parameterization. More recently, Cheng and Xu (2014) focused on the orientation of 2D CRMs based on three types of environments for mesoscale convective systems

* Presenting author address: Kuan-Ting Kuo, Department of Atmospheric Sciences, National Taiwan University, Taipei, Taiwan; e-mail: d09229002@ntu.edu.tw

(MCSs). Their results showed improvements in reducing biases in precipitation and circulation. Pritchard et al. (2014) examined the effects of horizontal scales on the Madden-Julian Oscillation (MJO), conducting experiments with CRM domain sizes of 32, 64, and 128 km. They concluded that CRM horizontal scales are not critical to MJO dynamics in SPCAM, but shortwave cloud forcing is enhanced for smaller CRM domain sizes in the tropics. Tao and Chern (2017) focused on CRM resolutions and grid points for simulating MCSs, finding that only higher resolutions (1 km or 2 km) and more grid points (128 and 256) could produce realistic MCSs. This improvement also affected the Hadley circulations and precipitation patterns.

These studies highlight differences among configurations, which can influence various weather systems differently. Configurations can be considered as different types of convective properties. Additionally, SPCAM has been employed in recent studies to develop machine learning-based convective parameterization (Gentine et al. 2018; Rasp et al. 2018; Mooers et al. 2021), as simulations provide realistic convective variability within the CRM under various large-scale environments. However, these studies used simulations with specific CRM configurations. It is worthwhile to explore how different types of sub-grid convection can yield different relationships with the large-scale environment, particularly in more extreme cases such as large-scale TC activities.

There are various experimental design approaches to investigate the effects of sub-grid configurations on TCs in SPCAM. One method involves conducting long-term climatology experiments to analyze the number of TCs or other TC-related statistics. Another approach is the short-term hindcast method, as employed by Ma et al. (2013, 2021). Their study illustrated that this approach could identify systematic biases arising from rapid moist processes within a few days by directly comparing with observational or reanalysis data. Patricola and Wehner (2018) adopted the hindcast method to simulate specific TC events and evaluate anthropogenic influences using pre-industrial and future projection forcings. Their findings suggested that the most intense TCs are projected to strengthen in a warmer climate, while changes in TC intensity between past and present climates were deemed insignificant. The short-term hindcast approach preserves a similar large-scale environment to the initial conditions, allowing for sensitivity experiments that are comparable with observations by diagnosing fast moist convective processes. Thus, we will conduct SPCAM hindcast experiments firstly to evaluate TC frequency under different CRM horizontal scales.

The paper is structured as follows: Section 2 describes the model and experiment design, including the hindcast setup and TC detection algorithm. The simulation and analysis results are presented in Section 3, followed by a summary and discussion in Section 4.

2. METHODOLOGY

2.1 Model and Experiments

The model used in this study is superparameterized CESM version 1.1.1. To simulate TCs in SPCAM, we use $0.9^\circ \times 1.25^\circ$ horizontal resolution and 30 levels in the vertical. The CRM resolution is 4 km with a periodic boundary condition, and the microphysics scheme is a single-moment scheme (Khairoutdinov and Randall, 2003; Khairoutdinov et al., 2005). The sensitivity of the coupling between convection and the large-scale environment is assessed by modifying the horizontal domain size of the sub-grid CRM. Three experiments are conducted by using domain sizes of 32, 128, and 1024 km with a 4-km horizontal resolution, and are denoted as D32, D128, and D1024, respectively. These experiments represent the degrees of freedom for convection to develop. The larger domain size is expected to allow a broader cloud spectrum or a more intense convective cloud to develop in a single timestep.

2.2 Hindcast setup

The hindcast experiment spans from June to September 2017, with daily initialization, resulting in a total of 122 initializations. Each experiment is integrated for 10 days, amounting to 1220 days of simulation. Initial conditions are derived from the fifth generation ECMWF atmospheric reanalysis (ERA5; Hersbach et al. 2020), while sea surface temperature (SST) and sea ice are prescribed using Optimum Interpolation SST (OISST) version 2.1 (Huang et al. 2021). This approach facilitates direct comparison with observational data, with each day of the simulation denoted from Day 0 to Day 9. Ensemble averages from specific hindcast days, such as Day 0 averaged across all 122 simulations, represent the 2017 summer average, with varying degrees of influence from initial conditions. Consequently, ensemble averages from Day 0 to Day 9 capture the transition from initial-condition dominance to model-intrinsic behavior.

Given that ERA5 serves as the basis for initial conditions, it is also partitioned into 122 10-day hindcast periods for validation purposes. The same procedure is applied to the Global Precipitation Measurement (GPM) IMERG product, which serves as precipitation validation data (Huffman et al., 2019).

2.3 Algorithm for Tropical Cyclones

To properly identify TCs in SPCAM, we adopt the definition established by Oouchi et al. (2006), with adjustments to enhance identification from ERA5 data. The criteria are outlined as follows:

- (1) The minimum sea-level pressure is at least 2 hPa lower than the average surface pressure over the surrounding $7^\circ \times 7^\circ$ grid box.
- (2) The magnitude of the maximum relative vorticity at 850 hPa exceeds $3.5 \times 10^{-5} \text{ s}^{-1}$.
- (3) The maximum wind speed at 850 hPa is larger than 15 m s^{-1} .

(4) The maximum wind speed at 850 hPa exceeds that at 300 hPa.

(5) The duration is not shorter than 36 hours.

(6) The surface pressure is below 1008 hPa.

(7) The objects whose minimum surface pressure falls below 880 hPa within the surrounding $5^\circ \times 5^\circ$ grid box are excluded.

(8) The SST is higher than 26°C for at least one timestep.

Grids satisfying the criteria and their neighboring grids are interconnected and tracked using a method outlined by Moseley et al. (2019). Criteria (1)-(5) are the same as Oouchi et al. (2006). Criterion (6) ensures a minimum TC strength. Criterion (7) can help filter out the topography. Criterion (8) confines tracks to those passing through tropical oceans, thereby excluding extratropical cyclones. These criteria are applied to both SPCAM experiments and ERA5 data with the exact resolution for a fair comparison. Figure 1 illustrates TCs diagnosed by this algorithm from the ERA5 data from 28 July 2017 to 5 August 2017. During this period, four TCs occurred, all accurately detected by the algorithm. However, there are occasional rare events that can complicate TC track identification. For example, Typhoons Haitang and Nesat merge into one TC by the algorithm at 01UTC on 30 July, then split after 3 hours. While this merge and split behavior may cause TC track shifts, it does not affect TC numbers or areas, which will be further analyzed in subsequent sections. The TC areas circled by color contours are the grids that pass the TC algorithm, and the TC tracks are the lines connecting the center of the TC areas.

3. RESULT

3.1 TC precipitation

Figure 2 shows the ensemble average of TC precipitation over the western North Pacific along the hindcast days. Each hindcast day represents the 2017 summer average, spanning from different days depending on the duration of the simulations (e.g., 20170601 to 20170930 for Day 0, and 20170610 to 20171009 for Day 9). The figure shows a systematic bias associated with the CRM horizontal scales. On Day 0, all experiments are close to the observation/reanalysis. However, in the later hindcast days, all experiments exhibit higher precipitation compared to the observation. Notably, D32 shows the most significant increase, with precipitation exceeding the GPM observation by over 0.3 mm h^{-1} on Day 8. In contrast, D1024 maintains a bias of less than 0.05 mm d^{-1} relative to the observation across the hindcast days. D1024 also exhibits a smoother transition, while precipitation in D32 and D128 sharply increases before Day 7. This increase can be contributed by more TCs or/and more intense rainfall by a single TC. Before analyzing the overall precipitation difference among the experiments, we will first demonstrate a TC

case to understand the TC simulations across different hindcast days.

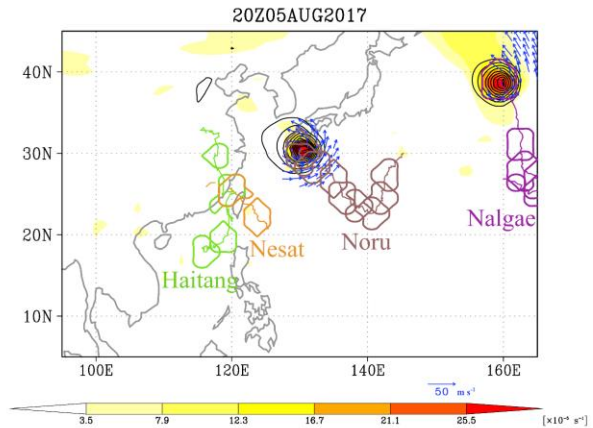


Figure 1. TCs diagnosed by the TC algorithm using ERA data. The shading is relative vorticity. The blue arrows are the wind field at 850 hPa and the magnitude stronger than 15 m s^{-1} . The black contour is sea-level pressure from 1000 hPa with a 2-hPa interval. The color contours and lines present TCs from 28 July 2017 to 5 August 2017. The interval of color contours is 24 hours. The names of TCs are labeled below the paths.

3.2 A case study for Typhoon Talim

With the hindcast approach, we can directly assess the performance of TC simulation in each experiment using a real TC case. For this purpose, we selected Typhoon Talim over the western North Pacific as an example. According to best track data from the Japan Meteorological Agency (JMA), Typhoon Talim was identified as a tropical depression at 20170908 12Z and strengthened into the typhoon category at 20170911 18Z. Figure 3 depicts the tracks of Typhoon Talim from ERA5 and in the experiments, with the closest TC identified within 900 km of the center of Typhoon Talim at 20170911 18Z marked with a typhoon symbol. The 900 km criterion was chosen to avoid confusion with Typhoon Doksuri, which locates around the south of Typhoon Talim. We selected the initial date 20170907 for analysis because it represents the earliest initialization when Typhoon Talim can be identified within the 10-day integration period in all experiments. Figure 4 illustrates the maximum wind speed at 850 hPa and precipitation rate within the defined area of Typhoon Talim. It is observed that Typhoon Talim is detected earlier in D32 compared to D128 and D1024. In D32, it intensifies more rapidly at the early stage, with maximum precipitation reaching 23 mm h^{-1} and maximum wind speed reaching 45 m s^{-1} , while in D1024, the corresponding values are only 6 mm h^{-1} and 24 m s^{-1} , respectively. This discrepancy indicates that, for Typhoon Talim, D32 intensifies earlier than in the other experiments and produces more rainfall. Although the TCs in D128 and D1024 intensify further at a later stage, there are variations in tracks and environments among the

experiments (Fig. 3), making direct comparison less suitable.

This case study highlights clear systematic differences in wind speed and precipitation among the experiments during the first four hindcast days. However, internal variabilities emerge later in the simulations. Consequently, the subsequent comparison will focus on the overall statistics of all tropical cyclones in the experiments.

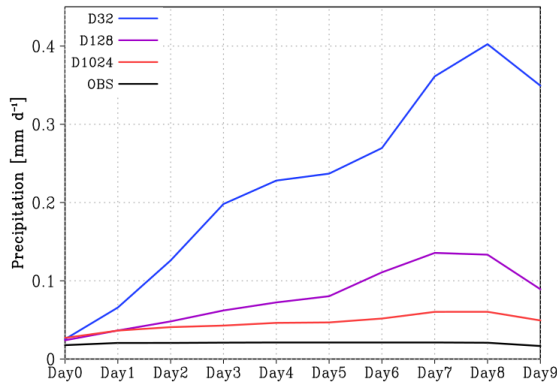


Figure 2. The ensemble average of TC precipitation over the western North Pacific (0° - 40° N, 100° E - 180° E) by each hindcast day. The blue, purple, and red lines represent experiments D32, D128, and D1024, respectively. The black line is observation, where precipitation is from the GPM, and TC areas are diagnosed from ERA5 data.

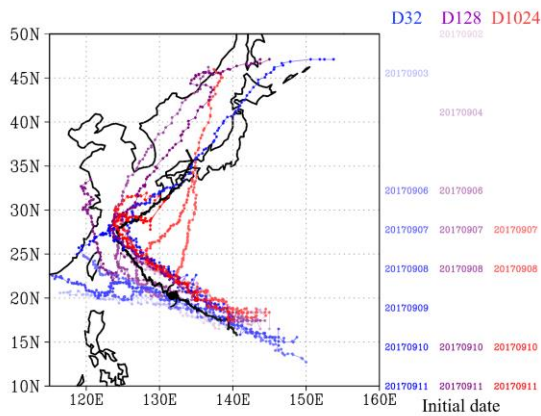


Figure 3. Diagnosed tracks of Typhoon Talim (2017). The red, purple, and red colors are experiments D32, D128, and D1024, respectively. The black color represents the diagnosed track from ERA5. The colors from light to dark represent the hindcast initial date from early to late.

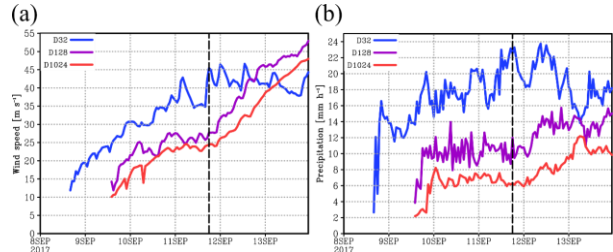


Figure 4. The hindcast runs initiated on 7 September 2017 of (a) maximum wind speed at 850 hPa and (b) maximum precipitation within Typhoon Talim. The dashed line illustrates the time of 18Z 11 September 2017, when Typhoon Talim intensified to typhoon category by the best track data from the Japan Meteorological Agency.

3.3 TC statistics

Table 1 presents the TC numbers and lifetimes in all experiments alongside the reanalysis data. ERA5 data is regridded to match the horizontal resolution of SPCAM and divided into 122 hindcast cases to align with the experiments. On average, D32, D128, and D1024 generate 8.07, 4.88, and 3.73 TCs per 10-day simulation, respectively, while only 3.42 TCs are diagnosed from ERA5. TC lifetimes do not differ significantly among the three experiments, all being shorter than ERA5 by approximately 10 hours.

Although D32 generates twice as many TCs as D1024, the strength of the TCs is not weaker. Figure 5 depicts the maximum 850-hPa wind speed and the maximum precipitation rate for each TC. The wind speed is higher in D32 than in D128 and D1024, and the spread (full range and interquartile range) is also more extensive. The precipitation rate shows a more significant difference among the three experiments. D32 can produce precipitation over 30 mm h^{-1} ; the average is over 5 mm h^{-1} higher than D128 and D1024. This result implies that the environment in D32 is more favorable for TC genesis and development.

Regarding spatial distribution (Fig. 6), all SPCAM experiments can generate TCs in the southern Indian Ocean, which does not exist in ERA5. The experiments also exhibit an excess of TC tracks around the central North Pacific, whereas no TC tracks are observed in the reanalysis data. This bias is weaker in D128 and D1024 but most severe in D32. In the South China Sea and the eastern Pacific, the TC track density of D32 is over 50 hours higher than the others. This result suggests that D32 produces more TCs likely due to a wider spatial distribution and higher occurrence frequency of TCs. It also explains why D32 yields more TC precipitation over the western North Pacific (Fig. 2).

Table 1. TC statistics of ERA5, D32, D128, and D1024

Exp.	ERA5	D32	D128	D1024
Total TC number	417	985	595	455
Number per 10 days	3.42	8.07	4.88	3.73
Average lifetime [hr]	103.81	95.22	90.54	95.85

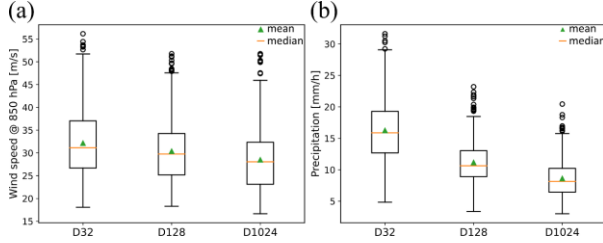


Figure 5. box plots of (a) Maximum wind speed at 850 hPa and (b) maximum precipitation for all TC events.

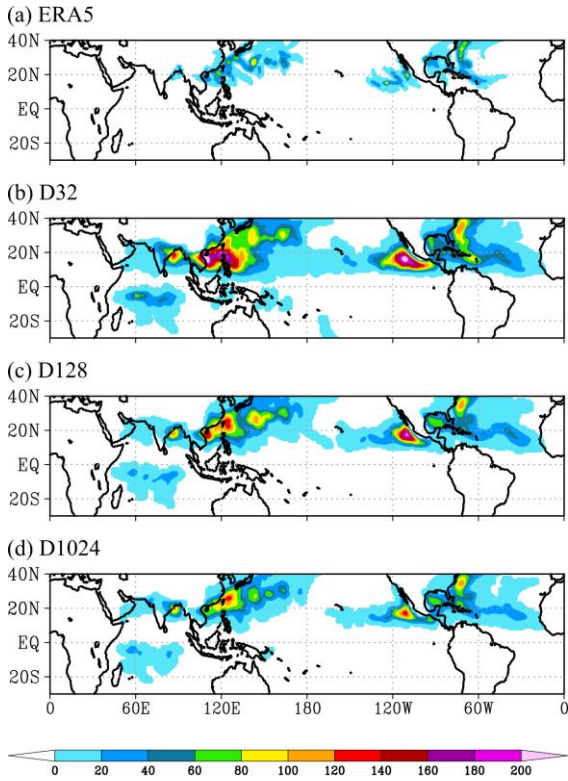


Figure 6. The ensemble average TC track density on the TC areas for (a) ERA5, (b) D32, (c) D128, and (d) 1024. The TC areas are defined as circled areas in Fig. 1. The unit is hours per summer (June - September).

3.4 Moisture Bias

TC genesis and TC tracks can be influenced by various factors, including SST, vertical wind shear, vertical instability, environmental vorticity, and humidity. Given our hindcast approach, some factors play a minor role in explaining the difference in TC genesis among the experiments. For instance, SST is consistent across all experiments, and the large-scale environment remains relatively stable during the 10-day hindcast experiments. Therefore, the convective process is the most significant factor influencing TC genesis within this short period.

A relative convective bias in SPCAM has been identified by Kuo and Neelin et al. (2020), who evaluated model biases of convective parameterization by analyzing precipitation rates as a function of column-integrated water vapor (CWV) and tropospheric temperature (T_{ave} ; equivalent to column-integrated saturation humidity in their paper). Their findings indicate that SPCAM exhibits a gentler slope for precipitation pickup with higher T_{ave} , and the CWV probability density functions (PDFs) extend to a high CWV regime under high T_{ave} . At the same time, it is close to observation for low T_{ave} . We apply the same analysis technique to our experiments, focusing on the CWV PDFs.

Figure 7 illustrates the CWV PDFs for observations and the three experiments across different ocean basins bounded by 20°S and 20°N. The colors represent different T_{ave} conditional samplings. In observation, the CWV PDFs increase rapidly between CWV values of 10 and 30 mm in the western Pacific (Fig. 7a). Then, the PDFs slowly increase (decrease) for high (low) T_{ave} . When CWV reaches a certain threshold, the PDFs drop sharply, indicating rapid moisture removal. The CWV PDFs in other ocean basins (Figs. 7e,i,m) exhibit similar patterns to those in the western Pacific. The dashed lines in Fig.7 roughly illustrate the upper bound of CWV PDFs for $T_{ave} > 271$ K in each ocean basin in observation. If a CWV PDF extends to a higher CWV regime, it suggests that the environment is wetter on average under the T_{ave} .

This moist bias becomes severe in D32 across the ocean basins (Figs. 7b,f,j,n), with unrealistic PDF peaks for CWV higher than the observation. In the Atlantic, for example, Fig. 7j exhibits a clear bifurcation for 273 K, and the CWV of a PDF peak is higher than the upper bound of observation (i.e., the dashed line), indicating an unstable environment. Similar biases are observed in the western and eastern Pacific, albeit with weaker bifurcations at 274 K and 273 K, respectively (Figs. 7b,f). In the Indian Ocean, while the bias of CWV PDFs extending into moister conditions persists, the bifurcation is less evident.

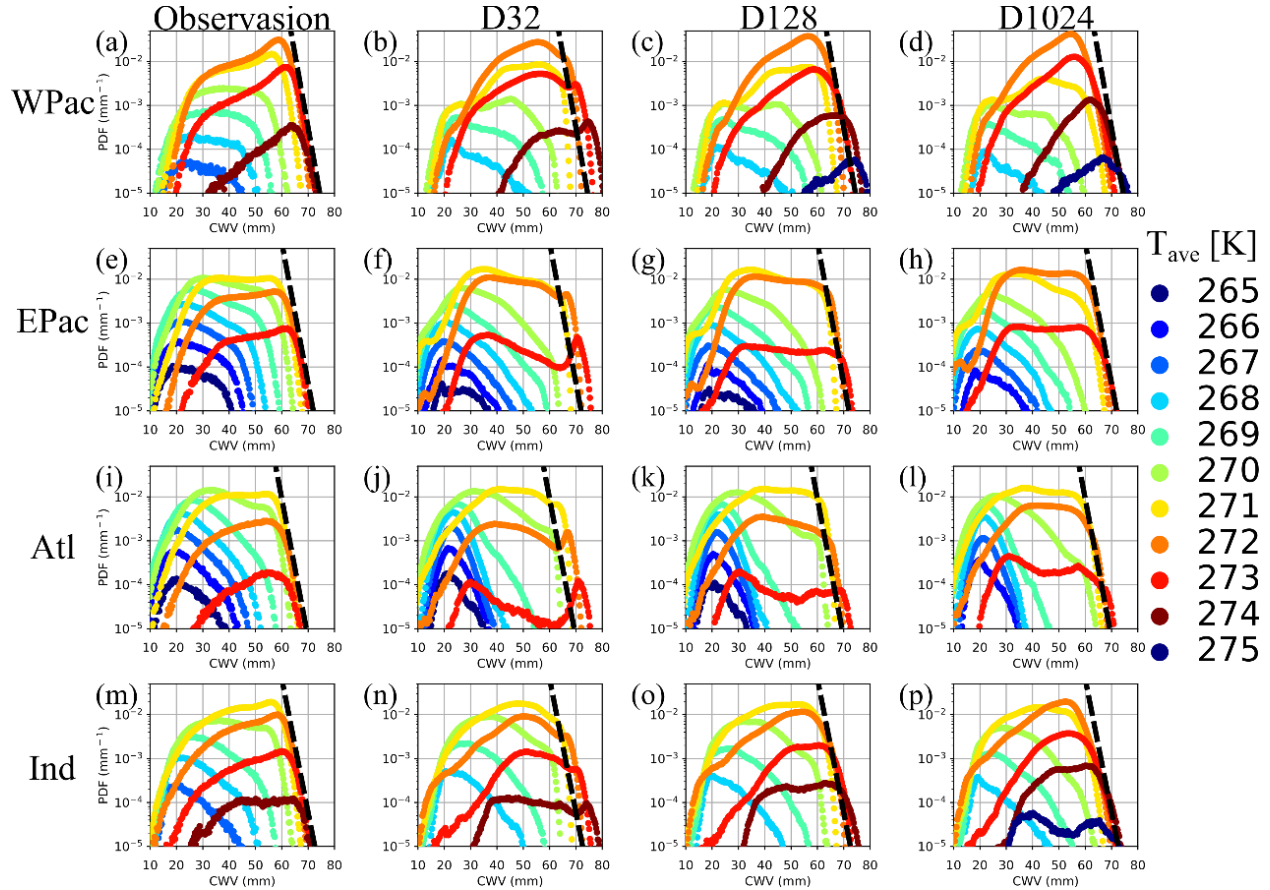


Figure 7. CWV PDFs for (a)(e)(i)(m) observations and experiments of (b)(f)(j)(n) D32, (c)(g)(k)(o) D128, and (d)(h)(l)(p) D1024 over (a)-(d) the Western Pacific, (e)-(h) the Eastern Pacific, (i)-(l) the Atlantic, and (m)-(p) the Indian Ocean within 20°S and 20°N. The colors mark the conditional samplings by the tropospheric temperature averaged between 1000 hPa and 200 hPa. The dashed lines illustrate the decline lines of the PDF in the observations in each ocean basin.

Conversely, D1024 performs better than D32 and D128. The upper bound of CWV PDFs closely matches observations in the eastern Pacific and Atlantic (Figs. 7h,l). For the western Pacific and the Indian Ocean, while the upper bounds are similar to observations, the peaks of CWV PDFs are lower, resulting in flatter slopes than observed (Figs. 7d,p). Generally speaking, the moist CWV bias in D1024 is small.

The CWV PDFs reveal a significant moisture bias of high CWV under high T_{ave} conditions for D32. Conversely, D1024 exhibits relatively reasonable CWV PDFs among all experiments. This result suggests that D32 is less efficient in adjusting convective instability. In the following subsection, we will focus on the spatial distribution of the event of high CWV under high T_{ave} conditions.

3.5 High T_{ave} -high CWV events and TCs

SPCAM exhibits unrealistically high CWV under high T_{ave} conditions, particularly evident in experiment D32. In

these high T_{ave} -high CWV regions, TCs are expected to play a significant role in moisture consumption and the maintenance of high T_{ave} , typically featuring a warm core structure. Figure 8 examines the occurrence probability for $T_{ave} > 271$ K and CWV > 70 mm and the probability of these events co-occurring with TCs. The left panel illustrates the spatial distribution of the probability of the high T_{ave} -high CWV events. These events are most frequent in the Bay of Bengal in both observations and simulations. Other regions, such as the eastern Arabian Sea, the western North Pacific, and the North Atlantic, also exhibit these events in observations. The SPCAM simulations reproduce a similar distribution but cover broader areas, especially in experiments with smaller CRM scales. Notably, these areas correspond to regions with a significant bias of TC track density (Fig. 6), including the South China Sea, the southern Indian Ocean, and the eastern North Pacific, and more severe for D32 in the central Pacific. The consistent spatial distributions suggest a possible relationship between the high T_{ave} -high CWV events and TCs.

CWV>70mm & T_{ave}>271K

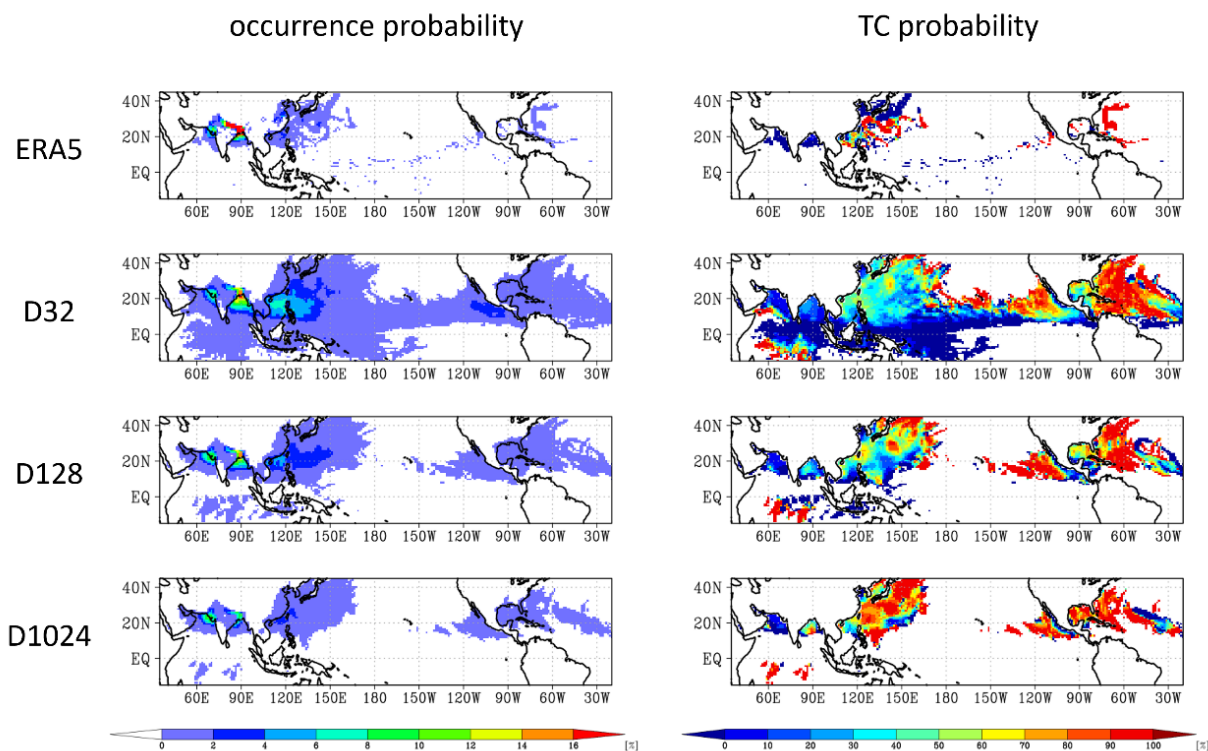


Figure 8. The left column is the occurrence probability for $CWV > 70$ mm and $T_{ave} > 271$ K. The right column is the occurrence probability of TCs under the high CWV and T_{ave} conditions.

The right panel of Fig. 8 presents the occurrence probability of TCs during the high T_{ave} -high CWV events. These events are typically associated with TCs in the western North Pacific and the North Atlantic in the observation. In the North Atlantic, this feature is consistent throughout all experiments. However, for experiments with smaller CRM domain sizes over the western North Pacific, this relationship appears weaker. The difference between the North Atlantic and the western North Pacific may be attributed to differences in the specific mechanisms of TC genesis. The environment in the North Atlantic is generally drier and colder than in the western North Pacific. TC genesis in the Atlantic is primarily linked to easterly waves, resulting in high T_{ave} -high CWV events due to TC-induced moisture convergence and convective heating. In contrast, TC genesis in the western North Pacific is more complex, involving other weather systems such as the MJO (Liebmann et al. 1994) and the summer monsoon (Wu et al. 2011). Moreover, the moist and warm environment in the western North Pacific typically leads to high convective instability. Therefore, TCs can either cause or result from high T_{ave} -high CWV events in this region.

Another perspective is that the high T_{ave} -high CWV events should occur primarily under strong convergence conditions such as those associated with TCs. A larger CRM domain can efficiently consume water vapor through deeper convection and the accompanied strong subsidence, meaning that only strong low-level water vapor convergence can accumulate CWV and maintain high T_{ave} . Conversely, in smaller CRM domains, convection may be less efficient in consuming water vapor, allowing CWV to accumulate rapidly even under weak convergence conditions. To further investigate the lower efficiency of convection in D32, we will examine the average mass fluxes for convective clouds in the experiments.

3.6 Convective clouds in CRMs

Mass fluxes of convective clouds offer insight into the environmental difference in different CRM domain sizes. We define convective clouds as the mixing ratio of cloud water and cloud ice is more than 10^5 kg kg⁻¹ for all levels within 2 km to 6 km, with vertical velocity is higher than 1 m s⁻¹. Figure 9 illustrates the average mass flux and cloud top height of convective clouds in each experiment.

D1024 shows the strongest mass flux and highest convective cloud top, while D32 exhibits the weakest mass flux and the lowest convective cloud top. This result suggests that horizontal scale influences convective cloud development, with smaller domain sizes limiting convection development, resulting in weaker vertical transport and lower convective cloud tops. This result is summarized in the schematic diagram in Fig. 10, illustrating the differences in cloud distribution between D1024 and D32 under convective conditions. In D1024, multiple convective clouds can coexist simultaneously, with strong convection extending deeper into the tropopause. Conversely, D32 can only accommodate one or a few convective clouds, which are weaker, with lower cloud top heights. Inadequate domain size can suppress convective cloud development, as a convective cloud may inhibit further growth through the compensating downdraft. Consequently, domain size constrains convective strength, leading to low efficiency in transporting water vapor from the boundary layer into the mid-troposphere and above. More water vapor will, therefore, accumulate within the boundary layer for the small CRM domain size, leading to higher CWV on average. Pritchard et al. (2014) also mentioned a similar effect. Their result emphasized on the difference in low clouds, while our result reveals the impact on convective clouds.

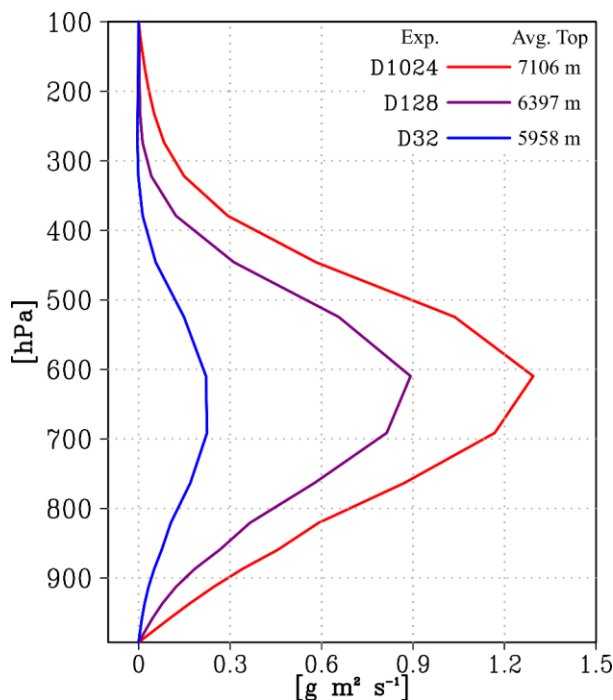


Figure 9. The mean mass fluxes for convective clouds. The convective clouds are defined as cloud water plus cloud ice $> 10^{-5} \text{ kg kg}^{-1}$ for all levels within 2 km to 6 km, and vertical velocity $> 1 \text{ m s}^{-1}$. The average convective cloud top height is labeled at the upper right corner for each experiment.

The inefficiency of sub-grid convection in consuming convective instability suggests that D32 requires additional large-scale forcing at the GCM scale to facilitate convective instability release, a role often played by TCs. However, within the SP framework, increased instability can only be advected because convective processes are confined to the sub-grid. Consequently, convective processes cannot rapidly adjust the high CWV bias in experiments with smaller CRM domains. Consequently, D32 exhibits more events and broader distribution of high T_{ave} -high CWV conditions.

4. SUMMARY AND DISCUSSION

This study carried out a set of hindcast experiments using SPCAM to examine the effects of sub-grid convection processes on TC statistics. A clear difference in the number of simulated TCs can be identified among three experiments for 32-, 128-, and 1024-km horizontal scales in CRMs of the SPCAM. More frequent and intense TCs are generated in the configuration with a smaller CRM domain size. To further link the changes in TC statistics to the sub-grid convective processes, we examined the CWV PDFs. There was a more severe moisture bias in D32 than in the other two experiments with a larger CRM domain, with more frequent high CWV events under warm tropospheric temperature conditions, leading to a very different relationship among CWV, temperature, and TCs. The statistics revealed the inefficiency to consume water vapor by convection when the CRM domain is small. This domain size dependence is also identified in the average convective mass fluxes, and the experiments with larger domain sizes exhibit stronger mass fluxes.

Naturally, TCs can be tightly associated with high T_{ave} -high CWV events. However, while most high T_{ave} -high CWV events in D1024 are associated with TCs, this correlation is weaker in D32. This suggests that most high T_{ave} -high CWV events in D1024 are induced by TCs, whereas D32 produces warmer and wetter environments more frequently due to the inefficient sub-grid water vapor removal, which is not directly related to TCs. We demonstrate that the larger CRM domain size exhibits more realistic CWV removal than the smaller one. This bias quickly accumulates in D32 because CWV can only be removed through the sub-grid processes under the SP framework. As a result, the frequent occurrence of high convective instability regions leads to more numerous TC genesis and development.

Our results also have an important implication for the convection parameterization based on SPCAM outputs using the machine learning method. Although the cloud-resolving approach captures the variability in convective structure more realistically than conventional parameterization, the results obtained in this study suggest that more variability can be generated by the CRM model configurations, especially in the extreme events such as tropical cyclones due to the strong convection-large scale interactions. For parameterization based on machine learning, the additional combination of

convection-large scale environment samplings provide the scenario for learning such interactions. This echoes Jones et al. (2019a; 2019b) that an ensemble approach is needed for the SPCAM to better represent climate variability. In addition, model physics in the embedded CRM can also play a role in modulating the convection-large-scale interactions. Huang and Wu (2020) demonstrated that even under a strong large-scale forcing, the simulated precipitation spectrum can be different when different microphysics schemes are adopted.

While we highlight numerous advantages of employing a larger CRM domain size, certain biases remain unaddressed. Notably, D1024 showcases a poleward shift of the Intertropical Convergence Zone (ITCZ) and South Pacific Convergence Zone (SPCZ), resulting in pronounced precipitation pattern discrepancies. This issue may stem from circulation alterations induced by non-uniform energy distribution. Idealized rotating aquaplanet experiments can offer further insights into the interplay between convection, circulation, and energy distribution across varying CRM configurations.

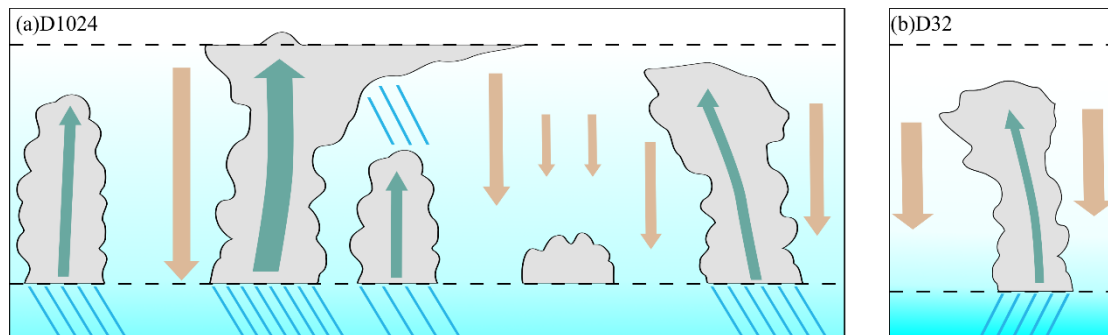


Figure 10. A schematic diagram adapted from a snapshot of the experiments (a) D1024 and (b) D32. The blue shading represents the water vapor mixing ratio. The green arrows represent the updraft of convection. The yellow arrows represent the compensating subsidence to convection. The bottom and top dashed lines represent the boundary layer and the tropopause, respectively.

REFERENCES

- Benedict, J. J., & Randall, D. A. (2009). Structure of the Madden–Julian Oscillation in the Superparameterized CAM. *Journal of the Atmospheric Sciences*, 66(11), 3277–3296. <https://doi.org/10.1175/2009JAS3030.1>
- Cheng, A., & Xu, K.-M. (2014). An explicit representation of vertical momentum transport in a multiscale modeling framework through its 2-D cloud-resolving model component. *Journal of Geophysical Research: Atmospheres*, 119(5), 2356–2374. <https://doi.org/10.1002/2013JD021078>
- DeMott, C. A., Randall, D. A., & Khairoutdinov, M. (2007). Convective Precipitation Variability as a Tool for General Circulation Model Analysis. *Journal of Climate*, 20(1), 91–112. <https://doi.org/10.1175/JCLI3991.1>
- DeMott, C. A., Stan, C., Randall, D. A., Kinter, J. L., & Khairoutdinov, M. (2011). The Asian Monsoon in the Superparameterized CCSM and Its Relationship to Tropical Wave Activity. *Journal of Climate*, 24(19), 5134–5156. <https://doi.org/10.1175/2011JCLI4202.1>
- Emanuel, K. (2021). Response of Global Tropical Cyclone Activity to Increasing CO₂: Results from Downscaling CMIP6 Models. *Journal of Climate*, 34(1), 57–70. <https://doi.org/10.1175/JCLI-D-20-0367.1>
- Gentine, P., Pritchard, M., Rasp, S., Reinaudi, G., & Yacalis, G. (2018). Could Machine Learning Break the Convection Parameterization Deadlock? *Geophysical Research Letters*, 45(11), 5742–5751. <https://doi.org/10.1029/2018GL078202>
- Held, I. M., & Zhao, M. (2011). The Response of Tropical Cyclone Statistics to an Increase in CO₂ with Fixed Sea Surface Temperatures. *Journal of Climate*, 24(20), 5353–5364. <https://doi.org/10.1175/JCLI-D-11-00050.1>
- Hersbach, H., Bell, B., Berrisford, P., Hirahara, S., Horányi, A., Muñoz-Sabater, J., et al. (2020). The ERA5 global reanalysis. *Quarterly Journal of the Royal Meteorological Society*, 146(730), 1999–2049. <https://doi.org/10.1002/qj.3803>
- Huang, B., Liu, C., Banzon, V., Freeman, E., Graham, G., Hankins, B., et al. (2021). Improvements of the Daily Optimum Interpolation Sea Surface Temperature (DOISST) Version 2.1. *Journal of Climate*, 34(8), 2923–2939. <https://doi.org/10.1175/JCLI-D-20-0166.1>
- Huang, J., & Wu, C. (2020). Effects of Microphysical Processes on the Precipitation Spectrum in a Strongly Forced Environment. *Earth and Space Science*, 7(6), 1–9. <https://doi.org/10.1029/2020EA001190>
- Huffman, G. J., E. F. Stocker, D. T. Bolvin, E. J. Nelkin, & Tan, J. (2019). GPM IMERG Final Precipitation

- L3 Half Hourly 0.1 degree x 0.1 degree V06.
<https://doi.org/10.5067/GPM/IMERG/3B-HH/06>
- Jones, T. R., Randall, D. A., & Branson, M. D. (2019a). Multiple-Instance Superparameterization: 1. Concept, and Predictability of Precipitation. *Journal of Advances in Modeling Earth Systems*, 11(11), 3497–3520.
<https://doi.org/10.1029/2019MS001610>
- Jones, T. R., Randall, D. A., & Branson, M. D. (2019b). Multiple-Instance Superparameterization: 2. The Effects of Stochastic Convection on the Simulated Climate. *Journal of Advances in Modeling Earth Systems*, 11(11), 3521–3544.
<https://doi.org/10.1029/2019MS001611>
- Khairoutdinov, M. F., & Randall, D. A. (2001). A cloud resolving model as a cloud parameterization in the NCAR Community Climate System Model: Preliminary results. *Geophysical Research Letters*, 28(18), 3617–3620.
<https://doi.org/10.1029/2001GL013552>
- Khairoutdinov, M. F., & Randall, D. A. (2003). Cloud Resolving Modeling of the ARM Summer 1997 IOP: Model Formulation, Results, Uncertainties, and Sensitivities. *Journal of the Atmospheric Sciences*, 60(4), 607–625.
[https://doi.org/10.1175/1520-0469\(2003\)060<0607:CRMOTA>2.0.CO;2](https://doi.org/10.1175/1520-0469(2003)060<0607:CRMOTA>2.0.CO;2)
- Khairoutdinov, M., Randall, D., & DeMott, C. (2005). Simulations of the Atmospheric General Circulation Using a Cloud-Resolving Model as a Superparameterization of Physical Processes. *Journal of the Atmospheric Sciences*, 62(7), 2136–2154. <https://doi.org/10.1175/JAS3453.1>
- Knutson, T., Camargo, S. J., Chan, J. C. L., Emanuel, K., Ho, C.-H., Kossin, J., et al. (2020). Tropical Cyclones and Climate Change Assessment: Part II: Projected Response to Anthropogenic Warming. *Bulletin of the American Meteorological Society*, 101(3), E303–E322.
<https://doi.org/10.1175/BAMS-D-18-0194.1>
- Kuo, K.-T., Chen, W.-T., & Wu, C.-M. (2020). Effects of convection-SST interactions on the South China Sea summer monsoon onset in a multiscale modeling framework model. *Terrestrial, Atmospheric and Oceanic Sciences*, 31(2), 211–225. <https://doi.org/10.3319/TAO.2019.08.16.01>
- Kuo, Y.-H., Neelin, J. D., Chen, C.-C., Chen, W.-T., Donner, L. J., Gettelman, A., et al. (2020). Convective Transition Statistics over Tropical Oceans for Climate Model Diagnostics: GCM Evaluation. *Journal of the Atmospheric Sciences*, 77(1), 379–403. <https://doi.org/10.1175/JAS-D-19-0132.1>
- Kuo, Y.-H., Schiro, K. A., & Neelin, J. D. (2018). Convective Transition Statistics over Tropical Oceans for Climate Model Diagnostics: Observational Baseline. *Journal of the Atmospheric Sciences*, 75(5), 1553–1570.
<https://doi.org/10.1175/JAS-D-17-0287.1>
- Liebmann, B., Hendon, H. H., & Glick, J. D. (1994). The Relationship Between Tropical Cyclones of the Western Pacific and Indian Oceans and the Madden-Julian Oscillation. *Journal of the Meteorological Society of Japan. Ser. II*, 72(3), 401–412.
https://doi.org/10.2151/jmsj1965.72.3_401
- Ma, H.-Y., Xie, S., Boyle, J. S., Klein, S. A., & Zhang, Y. (2013). Metrics and Diagnostics for Precipitation-Related Processes in Climate Model Short-Range Hindcasts. *Journal of Climate*, 26(5), 1516–1534.
<https://doi.org/10.1175/JCLI-D-12-00235.1>
- Ma, H.-Y., Zhou, C., Zhang, Y., Klein, S. A., Zelinka, M. D., Zheng, X., et al. (2021). A multi-year short-range hindcast experiment with CESM1 for evaluating climate model moist processes from diurnal to interannual timescales. *Geoscientific Model Development*, 14(1), 73–90.
<https://doi.org/10.5194/gmd-14-73-2021>
- Mooers, G., Pritchard, M., Beucler, T., Ott, J., Yacalis, G., Baldi, P., & Gentine, P. (2021). Assessing the Potential of Deep Learning for Emulating Cloud Superparameterization in Climate Models With Real-Geography Boundary Conditions. *Journal of Advances in Modeling Earth Systems*, 13(5), 1–26. <https://doi.org/10.1029/2020MS002385>
- Moseley, C., Henneberg, O., & Haerter, J. O. (2019). A Statistical Model for Isolated Convective Precipitation Events. *Journal of Advances in Modeling Earth Systems*, 11(1), 360–375.
<https://doi.org/10.1029/2018MS001383>
- Oouchi, K., Yoshimura, J., Yoshimura, H., Mizuta, R., Kusunoki, S., & Noda, A. (2006). Tropical Cyclone Climatology in a Global-Warming Climate as Simulated in a 20 km-Mesh Global Atmospheric Model: Frequency and Wind Intensity Analyses. *Journal of the Meteorological Society of Japan. Ser. II*, 84(2), 259–276.
<https://doi.org/10.2151/jmsj.84.259>
- Patricola, C. M., & Wehner, M. F. (2018). Anthropogenic influences on major tropical cyclone events. *Nature*, 563(7731), 339–346.
<https://doi.org/10.1038/s41586-018-0673-2>
- Pritchard, M. S., Bretherton, C. S., & DeMott, C. A. (2014). Restricting 32-128 km horizontal scales hardly affects the MJO in the Superparameterized Community Atmosphere Model v.3.0 but the number of cloud-resolving grid columns constrains vertical mixing. *Journal of Advances in Modeling Earth Systems*, 6(3), 723–739.
<https://doi.org/10.1002/2014MS000340>
- Pritchard, M. S., & Somerville, R. C. J. (2009). Assessing the diurnal cycle of precipitation in a multi-scale climate model. *Journal of Advances in*

- Modeling Earth Systems*, 2(4), 12.
<https://doi.org/10.3894/JAMES.2009.1.12>
- Randall, D., DeMott, C., Stan, C., Khairoutdinov, M., Benedict, J., McCrary, R., et al. (2016). Simulations of the Tropical General Circulation with a Multiscale Global Model. *Meteorological Monographs*, 56, 15.1-15.15.
<https://doi.org/10.1175/AMSMONOGRAPHS-D-15-0016.1>
- Rasp, S., Pritchard, M. S., & Gentine, P. (2018). Deep learning to represent subgrid processes in climate models. *Proceedings of the National Academy of Sciences*, 115(39), 9684–9689.
<https://doi.org/10.1073/pnas.1810286115>
- Roberts, M. J., Camp, J., Seddon, J., Vidale, P. L., Hodges, K., Vanni re, B., et al. (2020). Projected Future Changes in Tropical Cyclones Using the CMIP6 HighResMIP Multimodel Ensemble. *Geophysical Research Letters*, 47(14), 1–12.
<https://doi.org/10.1029/2020GL088662>
- Tao, W.-K., & Chern, J.-D. (2017). The impact of simulated mesoscale convective systems on global precipitation: A multiscale modeling study. *Journal of Advances in Modeling Earth Systems*, 9(2), 790–809.
<https://doi.org/10.1002/2016MS000836>
- Villafuerte, M. Q., Lambrento, J. C. R., Hodges, K. I., Cruz, F. T., Cinco, T. A., & Narisma, G. T. (2021). Sensitivity of tropical cyclones to convective parameterization schemes in RegCM4. *Climate Dynamics*, 56(5–6), 1625–1642.
<https://doi.org/10.1007/s00382-020-05553-3>
- Wu, L., Liang, J., & Wu, C.-C. (2011). Monsoonal Influence on Typhoon Morakot (2009). Part I: Observational Analysis. *Journal of the Atmospheric Sciences*, 68(10), 2208–2221.
<https://doi.org/10.1175/2011JAS3730.1>
- Zarzycki, C. M. (2022). Sowing Storms: How Model Timestep Can Control Tropical Cyclone Frequency in a GCM. *Journal of Advances in Modeling Earth Systems*, 14(3), 1–21.
<https://doi.org/10.1029/2021MS002791>
- Zhang, Y., Klein, S. A., Liu, C., Tian, B., Marchand, R. T., Haynes, J. M., et al. (2008). On the diurnal cycle of deep convection, high-level cloud, and upper troposphere water vapor in the Multiscale Modeling Framework. *Journal of Geophysical Research*, 113(D16), D16105.
<https://doi.org/10.1029/2008JD009905>
- Zhao, M., Held, I. M., & Lin, S.-J. (2012). Some Counterintuitive Dependencies of Tropical Cyclone Frequency on Parameters in a GCM. *Journal of the Atmospheric Sciences*, 69(7), 2272–2283. <https://doi.org/10.1175/JAS-D-11-0238.1>